VirtualBatteryFoam: A Multi-physics Numerical Solver to Simulate the Aluminium Electrolysis Process

Varchasvi Nandana[1], Roman Gutt[2], Hendrik Gesell[3], Alessandro Cubeddu[4], Roman Duessel[5] and Uwe Janoske[6]

1. Research Associate
2. Research Associate
3. Research Associate
4. Research Associate
6. Professor

Department of Fluid Mechanics, University of Wuppertal, Wuppertal, Germany

5. Department Manager, Reduction Area

TRIMET Aluminium SE, Essen, Germany

Corresponding author: nandana@uni-wuppertal.de

Abstract

Aluminium electrolysis is a very complex process consisting of various phenomena occurring in a highly coupled manner. A thorough understanding of the process is essential to enhance the cell efficiency and to reduce the production costs. Additionally, the shift towards renewable sources of energy demands for process and design flexibility. To realize the aforementioned goals, a detailed study of the process and the cell design is essential. Hence, in the present work, a numerical solver called "VirtualBatteryFoam" is developed in OpenFOAM® which can perform 3D cell simulations with fully solved physical phenomena. The solver consists of various models to capture magnetohydrodynamic and thermoelectric fields, electrochemistry with mass transfer, gas bubble dynamics and solidification process, capturing the evolution of ledge. In the first part, the numerical approach taken to develop the models is introduced. In the next part, verification of the various physical phenomena occurring in a typical cell including the long wave instability (sloshing), ledge formation and effect of gas layer formation on the electric field are presented.

Keywords: Aluminium electrolysis, numerical model, magnetohydrodynamics, thermoelectric field, OpenFOAM®.

1. Introduction

Aluminium production is a complex multi-scale, multi-physics process with a high degree of coupled non-linear dynamics. The process for production of aluminium is called Hall–Héroult process, which is named after its inventors who independently of each other developed and patented the electrolytic process in 1886. In this process, alumina (Al_2O_3) is dissolved in electrolytic bath mainly comprising of liquid cryolite (Na_3AlF_6) along with aluminium fluoride (AlF_3), calcium fluoride (CaF_2) and many other additives in small quantities, which is then subjected to a high electric current. The supplied electrical energy reduces the aluminium oxide to aluminium. The industrial process is carried out with prebaked carbon anodes, which is oxidized in parallel. The primary chemical reaction in its most simplistic form can be written as follows:

$$2Al_2O_3 + 3C = 4Al + 2CO_2 \quad (1)$$

A part of the dissolved aluminium reacts back with the CO_2 to produce Al_2O_3, thereby reducing the efficiency of the process. The back reaction can be written as:

$$2Al + 3CO_2 = Al_2O_3 + 3CO \quad (2)$$

Current efficiency, i.e., the ratio of actual amount of aluminium produced to the theoretical amount, is calculated with the help of the Faraday's law. The current efficiency in a typical aluminium cell ranges between 90 – 96 % [1, 2]. The gas (CO_2, CO) bubbles produced during the reduction process accumulate under the anode by coalescence, thereby influencing the local current density and the cell electrical resistance. The accumulated bigger bubbles pass in the bath and rise around the anode by displacing the bath at the ends and the sides. This release of gas bubbles creates circulation in the bath region resulting in the disturbance of the bath-aluminium interface.

High electric current in the range of 150 - 600 kA is supplied to a typical aluminium cell in the industry. At each cell, a voltage of 4 - 4.5 V occurs which can be attributed to decomposition potential, cathodic and anodic over-voltages, ohmic voltage drop in the cell and the external circuitry [1, 2]. A typical aluminium smelter has 100 – 450 electrolytic cells arranged in side-to-side or end-to-end configuration. Such huge electric currents create a strong magnetic field, generating Lorentz forces on the moving liquid metal and electrolytic bath inside the aluminium cell. Depending on the design of the external circuitry, distribution of the current density in the pot and the velocity field of the liquid metal itself, the Lorentz forces can stabilize the bath-metal interface or may sometimes lead to an unstable condition. The instability of the interface in extreme cases results in a short circuit when the liquid aluminium comes in contact with the anode surface. Additionally, the bubble dynamics influence the bath-aluminium interface and thereby affect the magnitude and orientation of the Lorentz forces in the cell. Hence it is vital to understand the magnetohydrodynamic (MHD) instabilities arising due to various cell parameters, so that the critical operating conditions of the cell can be established.

The high currents supplied to the cell generate huge amount of ohmic heat or popularly known as Joule heat. Typically, around 50 % of the supplied energy is lost as heat to the surroundings [1, 2]. The heat generated inside the pot facilitates the reactions to take place, as it maintains the required thermal environment. But a steep temperate gradient exists from the inside of the pot to the external surroundings. This temperature gradient leads to solidification of the molten cryolite around the internal linings of the cell. The solidified cryolite is called the ledge which protects the cell from the aggressive molten cryolite. The position of the ledge is dependent on various parameters like the applied current, the velocity field inside the cell and the composition of the electrolyte among many others. The ledge profile influences the cell chemistry and the cell hydrodynamics as well. The cell chemistry is influenced through the change in composition of the bath which in turn influences various physical properties of the bath. The ledge position affects the distribution of the electrical current density which in turn influences the Lorentz forces, thereby the velocity field and cell stability.

As evidently seen from the above discussions, all the phenomena in the aluminium reduction cell are strongly coupled with each other and a slight disturbance to any of the cell parameters can either lead to cell instability or the cell dynamics can stabilize itself. A numerical model capturing the main physical phenomena should help us understand the complex process. Through a systematic understanding of the underlying physics, process flexibility and increase in cell efficiency can be realised. The focus of the present work is to develop models to capture the distribution of temperature, electric current density, velocity field, gas bubble dynamics, aluminium production and MHD phenomena. This is realised through step-by-step development of various mathematical models to capture the complex physical process occurring in the cell. The goal of the project is to develop a single solver with all the mathematical models as shown in Figure 1.

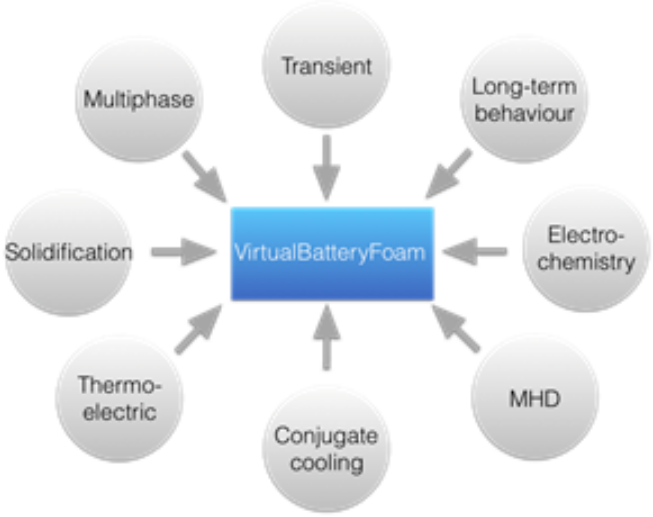

Figure 1. Schematic of the numerical solver "VirtualBatteryFoam".

2. Mathematical Model

In this section the various numerical models to describe the coupled problem of aluminium electrolysis are detailed. At first, the methods to model multiphase fluid system are presented, followed by the calculation of the electromagnetic field. Next, the numerical algorithm to capture the magneto-hydrodynamic phenomenon is introduced. The Faraday's electrochemical model to capture the production of aluminium, gases subsequently detailed in the third subsection. Lastly, the conjugate heat transfer model along with the melting model is described.

All the models are implemented in the framework of OpenFOAM®, which is an open source computational fluid dynamic (CFD) toolkit. To simulate the aluminium cell considering all the materials, a multi-region framework is essential. The multi-region conjugate heat transfer framework of OpenFOAM® is extended to the electric field computations enabling the thermal and electric field to be calculated in all the materials of the aluminium cell. The fluid field is modelled using multiphase approach which is described in the following subsection.

2.1. Multiphase Modelling

To model the multiphase flow system, two approaches are employed. In the first approach, the volume of fluid (VOF) method with phase-fraction based interface tracking model is used to capture the interface between aluminium and bath. For the VOF model the following assumptions are made:

- Aluminium and bath are treated as incompressible and immiscible fluids.
- Laminar flow conditions in the domain.
- Material properties in the domain are considered to be constant.

With the above-mentioned assumptions, the momentum conservation equation for laminar flows can be written as:

$$\frac{\partial \mathbf{u}}{\partial t} + \left(\mathbf{u}\cdot\nabla\right)\mathbf{u} = -\frac{\nabla p}{\rho} + \nu\nabla^2\mathbf{u} + S_u \tag{3}$$

Where $\mathbf{u}$ is the velocity vector, p is the pressure, ρ is the density, ν is the kinematic viscosity and S_u is the source term comprising of Lorentz force, gravitational force and Darcy type porosity term which will be addressed in the following subsection. The mass conservation for

incompressible fluids is given by $\nabla \cdot \mathbf{u} = 0$. The interface is tracked using a phase fraction α, which is defined as:

$$\alpha = \begin{cases} 0 = \text{fluid 1} \\ 0 < \alpha < 1 = \text{cell with interface} \\ 1 = \text{fluid 2} \end{cases} \tag{4}$$

The advection of phase fraction α is given by:

$$\frac{\partial \alpha}{\partial t} + \nabla \cdot (\alpha \mathbf{u}) = 0 \tag{5}$$

The energy conservation equation is given by:

$$\frac{\partial \rho E}{\partial t} + \nabla \cdot (\rho \mathbf{u} E) = \nabla \cdot (\lambda \nabla T) + S_E \tag{6}$$

where E is the total energy which is defined as the sum of the specific enthalpy and kinetic energy, λ is the thermal conductivity of the material and S_h is the volumetric source term. Applying the mixture approach in the framework of continuum model, the material properties are calculated as:

$$\psi = \alpha \psi_1 + (1 - \alpha) \psi_2 \tag{7}$$

where ψ_1 and ψ_2 are thermal and electric conductivities, specific heat capacity, kinematic viscosity and density of fluid 1 and fluid 2, respectively.

For the second approach, Eulerian model is implemented where gas bubbles are treated as dispersed phase whereas aluminium and bath are treated as continuous phase. In this approach, continuity and momentum equations are solved for each phase separately. The coupling between phases is achieved through the pressure and interphase exchange coefficients. The continuity equation for phase k, can be written as:

$$\frac{\partial \alpha_k}{\partial t} + \nabla \cdot (\mathbf{u}_k \alpha_k) = \sum_{p=1}^{n} \dot{m}_{pk} \tag{8}$$

where $\mathbf{u}_k$ is the velocity of phase k and $\dot{m}$ is the mass transfer from pth to kth phase. From the mass conservation one can obtain

$$\dot{m}_{pk} = -\dot{m}_{kp} \tag{9}$$

Similarly, the momentum conservation for phase k can be written as:

$$\frac{\partial \alpha_k \mathbf{u}_k}{\partial t} + \nabla \cdot (\alpha_k \mathbf{u}_k \mathbf{u}_k) + \nabla \cdot (\alpha_k R^{eff}) = -\alpha_k \frac{\nabla p}{\rho_k} + \alpha_k \mathbf{g} + \frac{M_k}{\rho_k} \tag{10}$$

where the R^{eff} is the combined Reynolds turbulent stress and viscous stress tensor, M_k is the averaged inter-phase momentum transfer. The inter-phase momentum transfer is the sum of drag, lift and virtual mass forces. Further details on Eulerian model can be found in [3, 4]. The pressure velocity coupled Navier-Stokes equations are solved using SIMPLE algorithm for

steady state simulations and PIMPLE, which is combination of PISO [5, 6] and SIMPLE algorithms, for transient simulations. The transport equations for phase fraction is solved using MULES (Multidimensional Universal Limiter with Explicit Solution) [4].

2.2. Electromagnetic Field Modelling

The main source of energy for the aluminium production is the electrical energy. The electric potential can be divided into static (Φ_0) and induced part (ϕ). The induced field arises due to moving metal in the magnetic field. With the assumption that free charges are non-existent in the system, the static potential can be calculated as:

$$\nabla \cdot \left(\sigma \nabla \Phi_0 \right) = 0 \tag{11}$$

where, σ is the electrical conductivity of the material. The above equation is solved in all the regions of the cell to determine the current density distribution. The induced part of the electric potential is calculated as:

$$\nabla \cdot \left(\sigma \nabla \phi \right) = \nabla \cdot \left(\sigma \left(\mathbf{u} \times \mathbf{B} \right) \right) \tag{12}$$

where **u** and **B** are the velocity and magnetic fields, respectively. The current density can be calculated from electric potential field as follows:

$$\mathbf{J}_0 = -\sigma \nabla \Phi_0 \tag{13}$$

$$\mathbf{j} = -\sigma \left(\nabla \phi + \mathbf{u} \times \mathbf{B} \right) \tag{14}$$

where $\mathbf{J}_0$ and **j** are the static and induced currents, respectively. The total current, **J** is the sum of the static and induced currents. Similarly, the Lorentz force can be calculated as shown below:

$$\mathbf{F} = \mathbf{J} \times \mathbf{B} \tag{15}$$

With the quasi static approach, the magnetic field required for the calculation of the Lorentz force are modelled using Gauss' magnetism law which states that the magnetic field must be the rotation of a vector potential, **A** defined as:

$$\mathbf{B} = \nabla \times \mathbf{A} \tag{16}$$

Together with Ampere's circuit law and Gauge transformation [7], the following formulation is obtained,

$$-\nabla^2 \mathbf{A} = \mu_0 \mathbf{J} \tag{17}$$

where μ_0 is the magnetic permeability of free space. To solve Equation (17) suitable boundary conditions are needed that are derived by combining Gauss' magnetism law with Biot-Savart law and can be written as:

$$\mathbf{A}\left(\mathbf{r} \right) = \frac{\mu_0}{4\pi} \int_V \frac{\mathbf{J}\left(\mathbf{r}' \right)}{\left| \mathbf{r} - \mathbf{r}' \right|} dV\left(\mathbf{r}' \right) \tag{18}$$

The above integral is performed only at the boundaries and Equation (17) is used to calculate the magnetic vector potential inside the domain. Once the vector potential **A** is known, the magnetic field, **B** can be calculated from Equation (16). The aforementioned method, where the

internal magnetic vector potential field is computed from Ampere's circuit law, reduces the computational effort significantly when compared with computing the whole domain with Biot-Savart law. Further information on the modelling can be found in [8].

2.3. Magnetohydrodynamics

The magnetohydrodynamic modelling is obtained by solving the Navier-Stokes equation (Equation 3) with Lorentz and gravitational forces as source terms. The electric current density and magnetic field required to calculate the Lorentz force are obtained by solving the electromagnetic field equations, both of which are described in previous subsections. The algorithm to calculate the MHD instabilities is depicted in Figure 2.

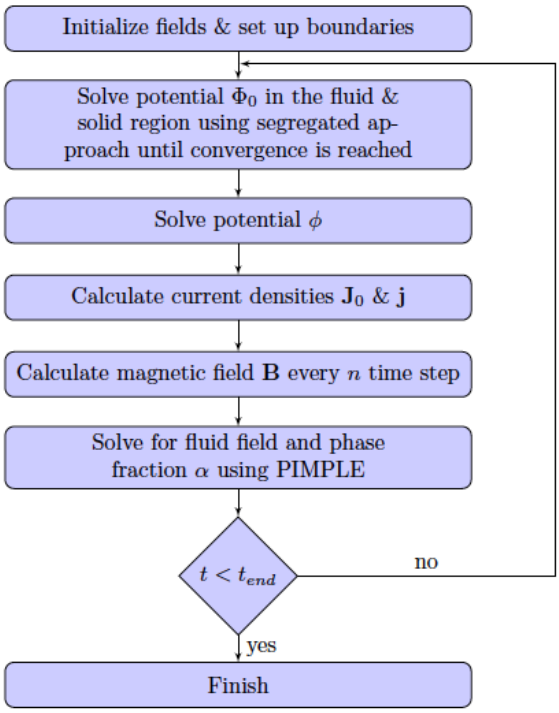

Figure 2. Flowchart depicting the numerical algorithm of the MHD solver.

2.4. Electrochemistry and Mass Transfer Modelling

The production of aluminium, CO_2 and CO along with the consumption of Al_2O_3 are modelled with the simple Faraday's law of electrolysis. According to the law, the rate of mass production, $\dot{m}$ of a substance at the electrode (kg/s) and is given by:

$$\dot{m} = \frac{IM}{1000Fz} \tag{19}$$

where I is the current passing through the electrode in kA, M is the molar mass of the substance, F is the Faraday constant (96 485.332 8959 C/mol) and z is the valency number of the ions of the substance. Substituting the molar mass (= 26.9815384 g/mol) and valency number for aluminium (=3), carbon, CO_2 and Al_2O_3, one obtains the following theoretical mass production/consumption rates:

$$\dot{m}_{\ldots} \qquad 14646\times10^{-5} I \tag{20}$$

$$\dot{m}_{CO_2} = 1.223331\ \dot{m}_{Al} \tag{21}$$

$$\dot{m}_{C} = 0.333867\ \dot{m}_{Al} \tag{22}$$

$$\dot{m}_{Al_2O_3} = \dot{m}_{Al} \tag{23}$$

where $\dot{m}$ is in kg/s and I is in kA. The consumption of alumina and carbon as well as the production of CO_2 are expressed relative to production of aluminium.

2.5. Thermoelectric Model

The temperature field is obtained by solving the energy equation in all the regions of the aluminium reduction cell. For solid materials, the energy conservation equation can be written in terms of specific enthalpy as:

$$\frac{\partial \rho h}{\partial t} = \nabla \cdot \left(\lambda \nabla T \right) + S_h \tag{24}$$

The pot region consisting of aluminium and electrolyte is modelled with VOF approach and the energy equation is already described in subsection 2.1. For thermoelectric calculations, the joule energy is modelled as an explicit volumetric source term for both solid and pot regions and is given by:

$$S_h = \frac{\mathbf{J}^2}{\sigma} \tag{25}$$

2.5.1. Modelling of Ledge

To capture the evolution of ledge in the pot region, a phase change or solidification model is implemented. The solidification model is based on the framework of enthalpy-porosity method developed by Swaminathan and Voller [9]. For two fluid system, the VOF approach is extended to capture the phase change process of the electrolyte. This is achieved by defining another phase fraction called melt (γ) and defined as:

$$\gamma = \begin{cases} 0 & \text{if} \quad T < T_s \\ \frac{T - T_s}{T_l - T_s} & \text{if} \quad T_s \leq \mathrm{T} \leq T_l \\ 1 & \text{if} \quad T > T_l \end{cases} \tag{26}$$

Here T_l is the liquidus temperature and T_s is the solidus temperature of the electrolyte. The transition from solid to melt electrolyte is for simplicity assumed to be a linear function. According to Equation (26), γ =1 denotes melt electrolyte and 0 denotes solid electrolyte. With the above definition, the specific enthalpy of the mixture can be written in terms of temperature as:

$$h = C_p T + \alpha \gamma L \tag{27}$$

where C_p and L are the specific heat capacity of the mixture and latent heat of solidification of electrolyte, respectively. Substituting Equation (27) in Equation (6), one obtains

$$\frac{\partial \rho T}{\partial t}+\nabla\cdot\left(\rho \mathbf{u} T\right)+\frac{\partial \rho K}{\partial t}+\nabla\cdot\left(\rho \mathbf{u} K\right)=\nabla\cdot\left(\frac{\lambda}{C_p}\nabla T\right)+\frac{\mathbf{J}^2}{\sigma}-\alpha\frac{L}{C_p}\left[\frac{\partial(\rho\gamma)}{\partial t}+\nabla\cdot\left(\rho\gamma\mathbf{u}\right)\right] \tag{28}$$

The effect of solidification on velocity field is modelled with the help of Darcy type source term in Equation (3). The pressure gradient inside the mushy zone is coupled to the permeability using the modelling of Kozeny-Carman equation [10] which can be written as:

$$S_u=\alpha C\frac{\left(1-\gamma\right)^2}{\gamma^3}\mathbf{u} \tag{29}$$

where, C is an empirical constant. Extending the mixture approach to solid and melt phase fraction, the physical properties of the mixture can be calculated as follows:

$$\psi=\alpha\left(\gamma\psi_{melt}+\left(1-\gamma\right)\psi_{solid}\right)+\left(1-\alpha\right)\psi_2 \tag{30}$$

The melt fraction and energy equations are coupled in a non-linear fashion requiring an iterative process to compute the temperature field and ledge position. The iterative process can be computationally expensive, and the problem is circumvented by defining a switch function to include the melt fraction source terms in the energy equation only when temperature lies in the range where phase change occurs. The details of the implementation can be found in [11].

3. Numerical Results

In this section, the numerical results of various phenomena that occur in a typical aluminium cell are presented. In the first subsection, the metal pad rolling instability is detailed and the verification of the numerical model with experimental data is presented. Next, the production of gases is shown along with bubble dynamics. In the last section, the thermoelectric field with the position of ledge is discussed.

3.1. Metal Pad Rolling

The metal pad rolling instability is a well-known phenomenon in Hall–Héroult cell. The mechanism explaining the origin of metal pad rolling was first given by Sele [12]. The strong electric currents in the external circuits of the cell generate a magnetic field inside the cell, which here is termed as external magnetic field, B_{ext}. The B_{ext} together with the electric current density in the pot result in Lorentz force, which is responsible for the rolling of the metal pad.

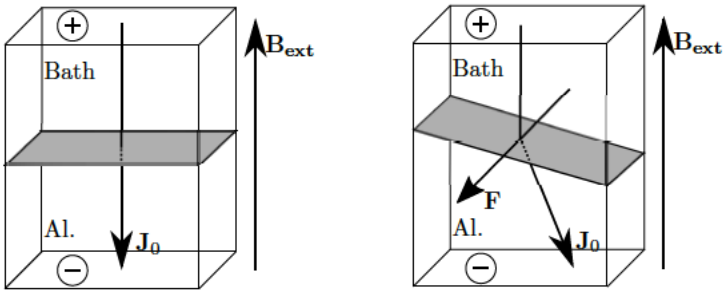

Figure 3. Schematic of a simplified aluminium cell with horizontal (left) and disturbed (right) interface.

For simplification, consider Figure 3 as a simplified aluminium cell with J_0 as the static current and B_{ext} as the external magnetic field. In the undisturbed state of the cell, where the interface of electrolyte-aluminium is horizontal, no Lorentz force exists as the cross product of both the vectors lead to zero. In reality, the interface is never flat, which results in a horizontal component of the J_0. The horizontal component generates Lorentz force by interacting with B_{ext}, resulting in wave like motion of the fluids in the cell. Along with the Lorentz force, the reflection of the wave from the walls result in what is well known as the metal pad rolling or sloshing, which can be seen in Figure 4. The sloshing in Figure 4 is depicted at 5 different time steps. A small perturbation in the interface creates a perturbed current which always flows from a crest (red) of aluminium to trough (blue) resulting in a Lorentz force which is orthogonal. The orthogonal Lorentz force displaces the aluminium in the direction of the force. When the fluid meets a wall, the wave is again reflected orthogonally, thereby resulting in rotation of the wave. If the work done by Lorentz force is larger than ohmic and viscous dissipation, we can expect the amplitude of the wave to grow.

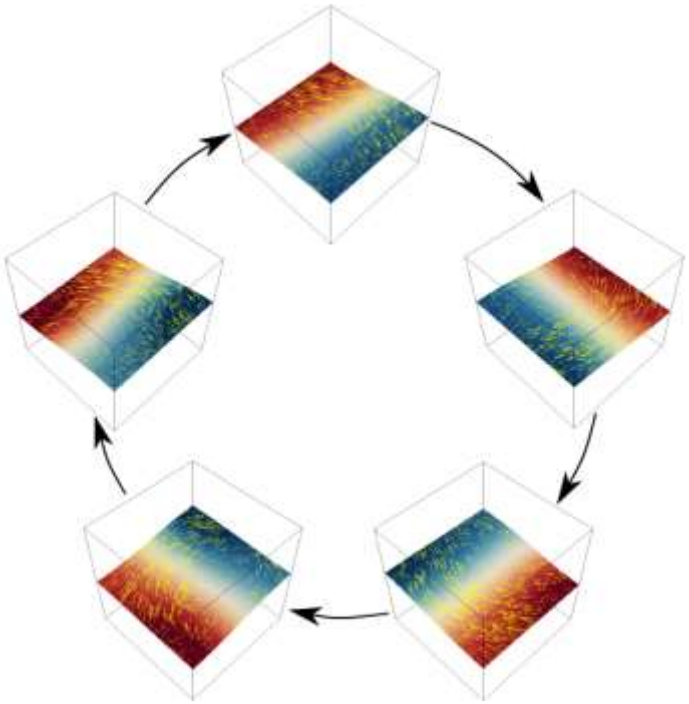

Figure 4. One cycle of metal pad rolling in the simplified aluminium cell.

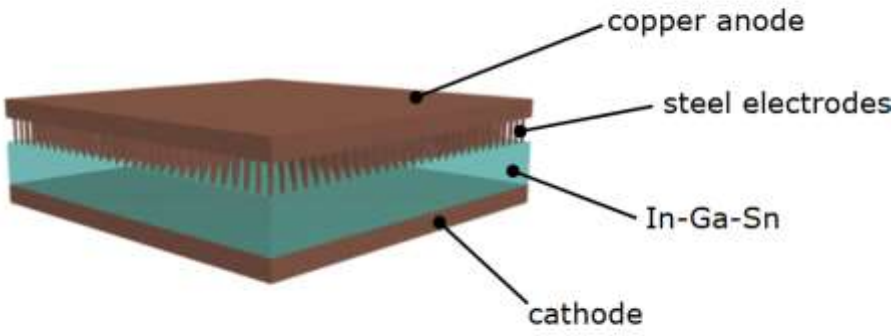

Figure 5. Schematic of the numerical domain.

The verification of the numerical model is done by comparing the amplitude of the metal pad rolling with the experiments conducted by Pedchenko et al. [13]. The schematic of the numerical domain is shown in Figure 5. The domain consists of copper anode at the top followed by a total of 900 steel electrodes inserted in the cell containing water at the top and liquid galistan (In-Ga-Sn) at the bottom. The cathode which is made of steel is placed at the bottom of the cell. The height of the steel rods is such that when the interface is horizontal, the rods are slightly immersed in galistan. The idea behind the setup is to simulate the vertical current in electrolyte of a typical aluminium cell. The galistan metal here simulates the behaviour of the liquid aluminium. More details on the experiment can be found in [13].

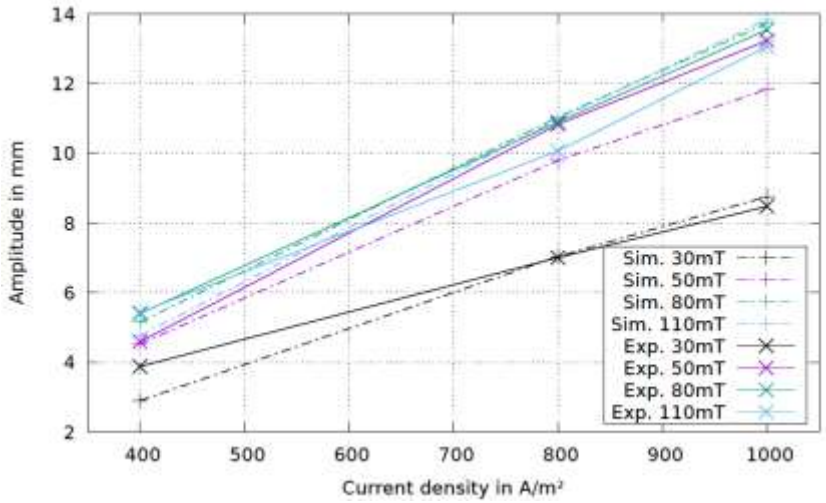

Figure 6. Comparison of amplitudes between numerical simulations and experiments [13].

In the numerical simulations, the rods are fully resolved to accurately capture the electric current density and damping of the wave. For ease of computation, the anode material is considered to be the same as electrode rods. The simulations are carried out with three separate regions consisting of the anode with rods, the cell region consisting of galistan and water and finally the cathode. A uniform current density at the top of the anode and zero potential at the bottom of the cathode are set as boundary conditions for electric field. All other boundaries are treated as electrically insulated. For fluid simulations in the multiphase region, all boundaries are treated as walls. The fluids are assumed to be incompressible, immiscible and laminar. The simulations are carried out for current densities ranging from 400 A/m^2 to 1000 A/m^2 and B_{ext} ranging from 30 mT to 110 mT. The amplitude of the interface is tracked and are compared with the experimental results of [13] as shown in Figure 6. It is evident that the amplitudes of the sloshing instabilities predicted by numerical simulations are in very good agreement with the experiments, thus verifying the numerical model. The small discrepancies can be attributed to the various assumptions made for the numerical calculations. In the next step, the focus is to separate the anode from the rods, include the effect of surface tension forces and consider the inclusion of external connections for anode and cathode for the calculation of the magnetic field.

3.2. Electrochemistry and Bubble dynamic

The modelling of Faraday's law and bubble dynamics are verified here with the experimental works of Zhao et al. [14]. The schematic of the experiment is shown in Figure 7a. In the current experimental setup, aluminium is not included. Electric current is supplied through anode to the electrolyte chamber which later flows out through the cathode. The electrolyte chamber is separated into a larger anode chamber and a smaller cathode chamber. The gas CO_2 is produced in the anode chamber under the anode. For various anode current densities, the build-up and

release dynamics of gas bubbles and its effect on the cell's voltages are studied. Numerical simulations using Euler-Euler model with CO_2 treated as dispersed phase and electrolyte as continuous phase are carried out in the current work (Section 2.1). CO_2 production is modelled using Faraday's law of electrochemistry (Section 2.4). For the present simulation, only the electrolyte chamber is considered with a zero potential at the anode boundary and uniform electric current density at the cathode boundary. For ease of computation, 2D assumption is made for the numerical calculation. In the future, the simulations are planned to be extended to 3D geometry with anode and cathode materials included as separate regions such that the computation of the electric field is more accurate.

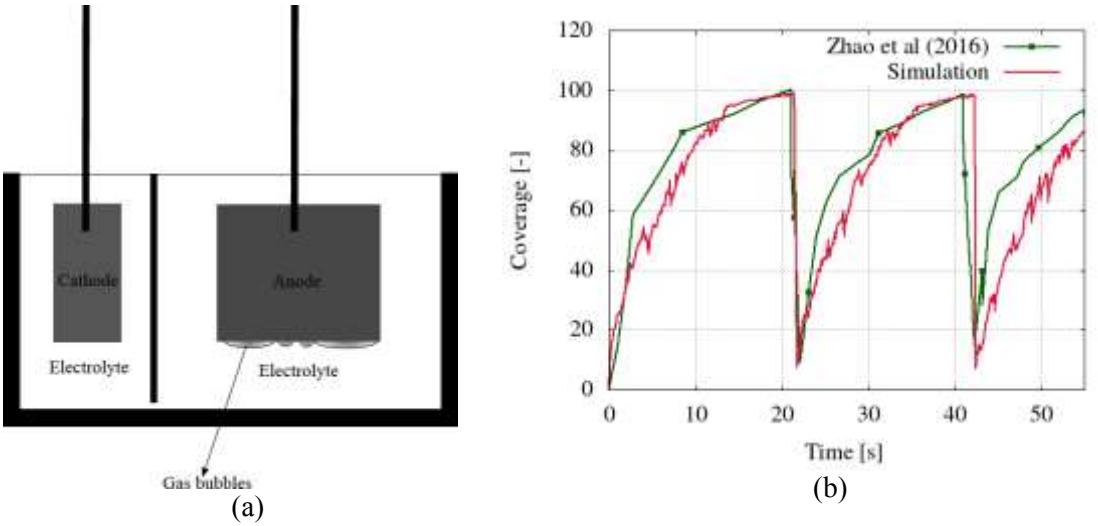

Figure 7. Figure showing experimental setup (a) and numerical result of coverage dynamics for a current density of 0.5 A/cm^2 (b).

Firstly, there is always a minimum amount of gas bubbles adhering to the bottom surface of the anode, as the coverage never goes to 0 %. Marching further in time, the small bubbles combine with other smaller bubbles produced, resulting in larger bubbles. The increase in bubble coverage with minor fluctuations in growth explains the period where bubble coalescence occurs. Once a single bubble covering the whole surface is formed, the bubble grows in depth for some period. In the last stage, the bubble is released as it reaches a critical coverage depth resulting in residual small bubbles. For lower current densities and assuming no other sources of disturbance in the electrolyte region, the aforementioned cyclic process continues.

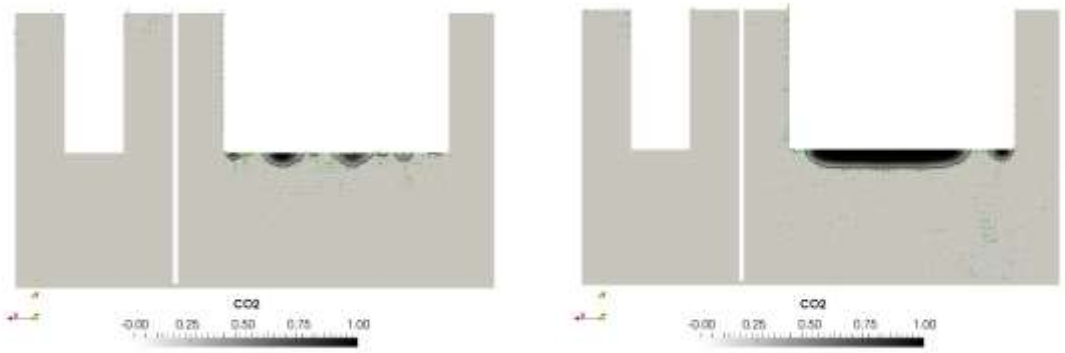

Time = 1.5 s Time = 9.5 s

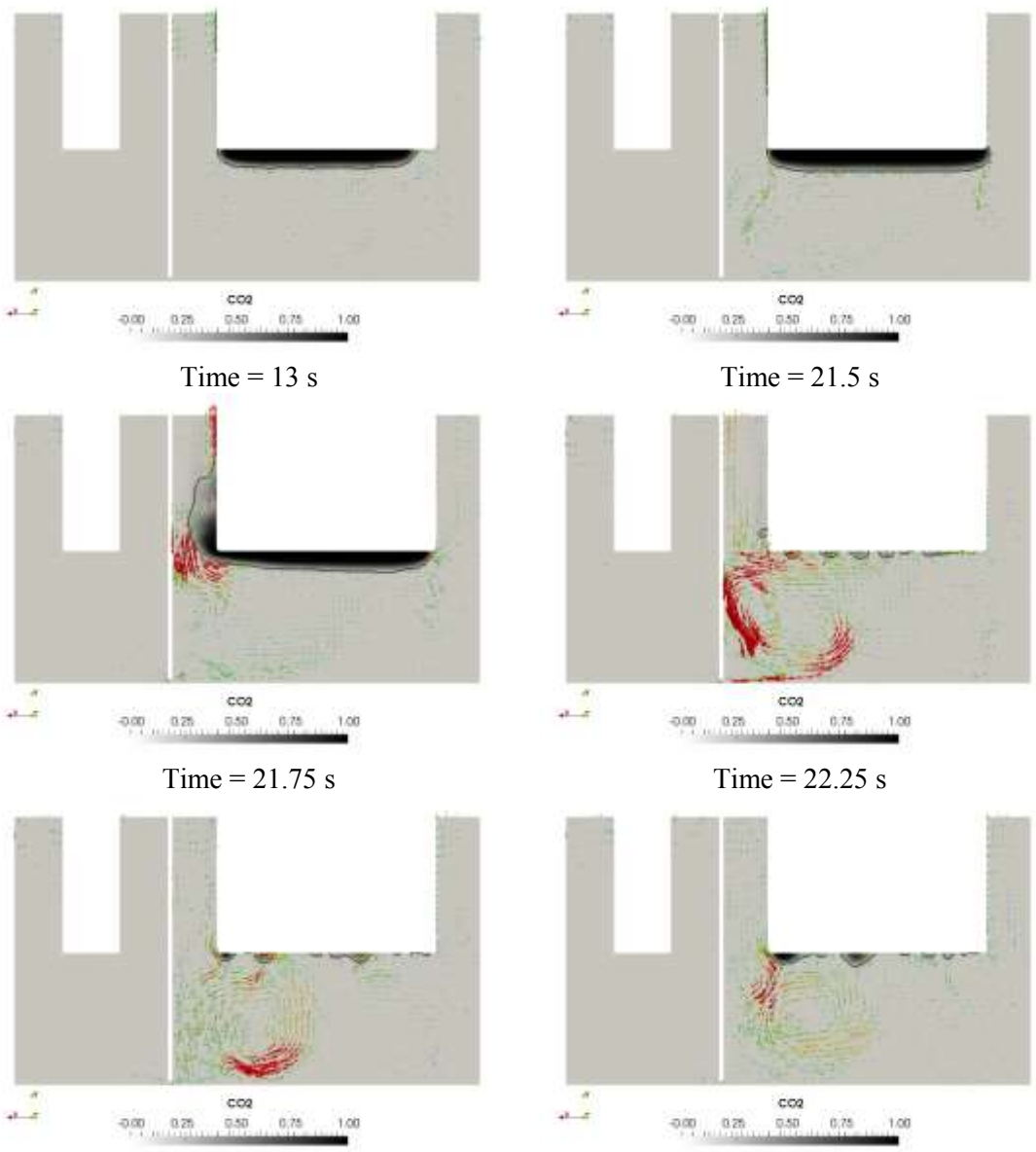

Figure 8. Cyclic dynamics of bubble growth and release with velocity vector plot.

The cyclic phenomenon with bubble dynamics and its influence on the electrolyte disturbance can be clearly seen in Figure 8. At time t = 1.5 s, the small bubbles are produced which combines to form bigger bubbles (t = 9.5 s) until one single bubble mass is formed under the anode (t = 13 s). After this stage, the bubble depth starts to grow until a critical value is reached, which in our simulation occurs at t = 21.5 s. Once the depth increases beyond the critical value, a release of the bubble occurs. The released bubble flows out of the system though the top displacing the electrolyte, which can be clearly seen occurring at t = 21.75 s. After the release, small residual bubbles continue to adhere to the anode's bottom surface and further production of the CO_2 occurs with the cycle continuing. Additionally, the disturbance is damped after a period of approximately 2 s, which amounts to 10 % of the cyclic period. The bubble release period in simulation and experiment [14] are 21.5 s and 21.25 s, respectively. The coverage height in simulation and experiment are 5mm and 4.1mm, respectively. The coverage percentage between simulation and experiment are in very good agreement with both lying in the range of 98 – 99 %. The result verifies the Faraday's model for mass production and the

Euler-Euler approach for bubble dynamics in multiphase framework, thus asserting confidence in both the models.

3.3. Thermoelectric Field and Ledge Profile

The calculation of temperature and electric current density distribution in an aluminium cell is important to understand the cell dynamics. The position of ledge in the cell is a critical parameter to assess the optimal functionality of the cell. Hence in the current section, the thermoelectric field calculations with prediction of ledge position is qualitatively presented.

The calculation of ledge position is done using the enthalpy-porosity method as mentioned in Section 2.5. To validate the model, an experimental setup was constructed with paraffin (Rubitherm® RT35) and air as two fluids, where paraffin undergoes phase transformation from solid to liquid and vice versa. Paraffin is filled in the chamber up to a certain height and the remaining volume is taken by air. The chamber is heated to a fixed temperature from one of the side walls and all other walls are insulated. The schematic of the setup can be seen in Figure 9a. Plexiglass material is used for the construction of the chamber as it would be easy to track the interface of the paraffin. After the start of the experiment, pictures are taken at regular intervals to track the melt interface. The position of the interface is extracted from the pictures using a digitizer tool. The experimental results are then compared with the numerical simulations which are carried out in multiphase framework as shown in Figure 9b. The interface positions at various time intervals predicted by the simulation are in excellent agreement with the experimental results, thus validating the model. Further information on the results can be found in [11].

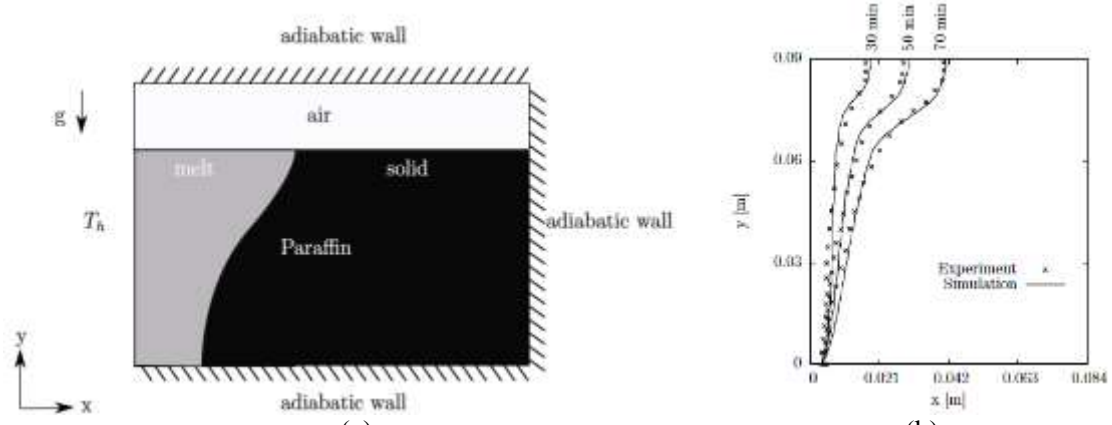

(a) (b)

Figure 9. Schematic showing the numerical domain (a) and comparison between experimental results and numerical simulation for T_h = 44 °C (b).

In the next step, simulations of a section of aluminium cell containing one anode are carried out using the thermoelectric model. The details of the numerical model are already described in Section 2. The geometry of the cell considered for numerical simulations is as shown in Figure 10. It contains in total 14 regions, including the pot with bath and aluminium, anode, cathode, collector bars, insulating materials anode bar and yoke among others. The simulations are carried out with uniform electric current density at the top of the anode bar and zero potential given at the cathode collector bar. For temperature boundary conditions, the external walls of the cell are set to the boundary condition replicating the convective heat transfer occurring at the walls in an industrial cell. The effect of radiation is considered in the convection coefficient of the convective heat transfer boundary condition. Since the magnetic field calculations are not carried out in the present simulations, no convection occurs in the cell. To include the effect of

convection, a high heat conduction constant is employed for liquid aluminium and liquid electrolyte.

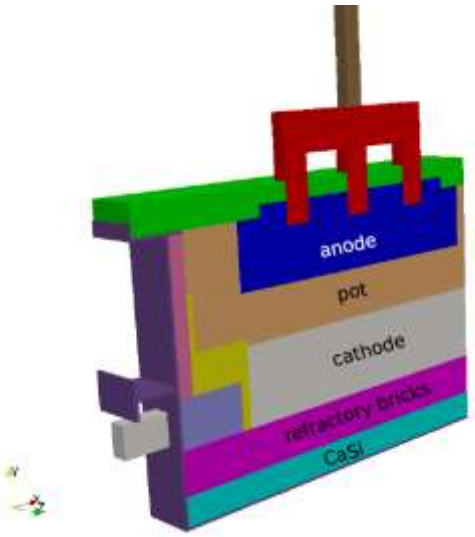

Figure 10. Computational domain of an aluminium cell

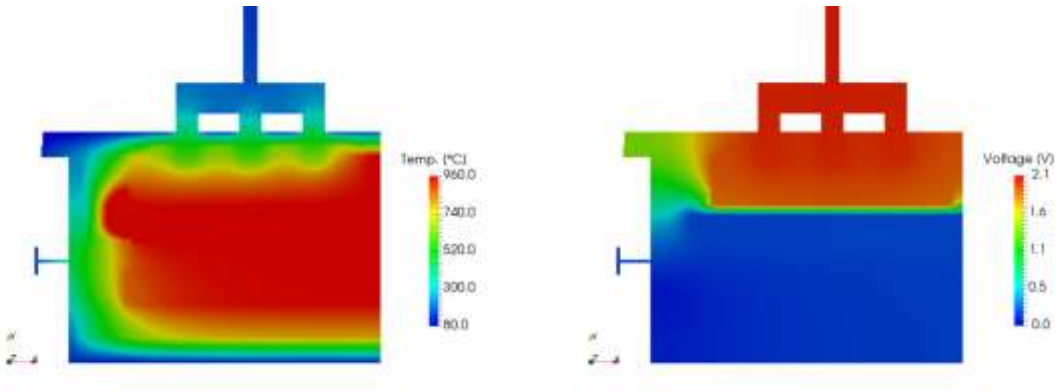

(a) (b)

Figure 11: Contour plot showing temperature distribution (a) and voltage distribution (b) in a 2D section of the aluminium cell.

With the aforementioned boundary conditions and model assumptions, the thermoelectric field calculations are carried out for line currents 150 kA, 155 kA, 162 kA, 170 kA and 180 kA. In Figure 11 the temperature and voltage distribution contours for 162 kA can be seen. One can observe the steep temperature gradients at the side wall, which is the region containing ledge and at the bottom, where the cell is insulated from layers of insulating materials. In Figure 11b, the voltage drop in the electrolyte can be seen, which is the highest in the cell. The ledge position for various line currents are shown in Figure 12. It is clear that as line current increases, the ledge moves closer to the wall linings. And in the present geometry, for a line current of 150 kA, the isotherm moves below the anode which is clearly not good for cell operations. Additionally, one can observe the formation of ledge toe for line current 150 kA and 155 kA.

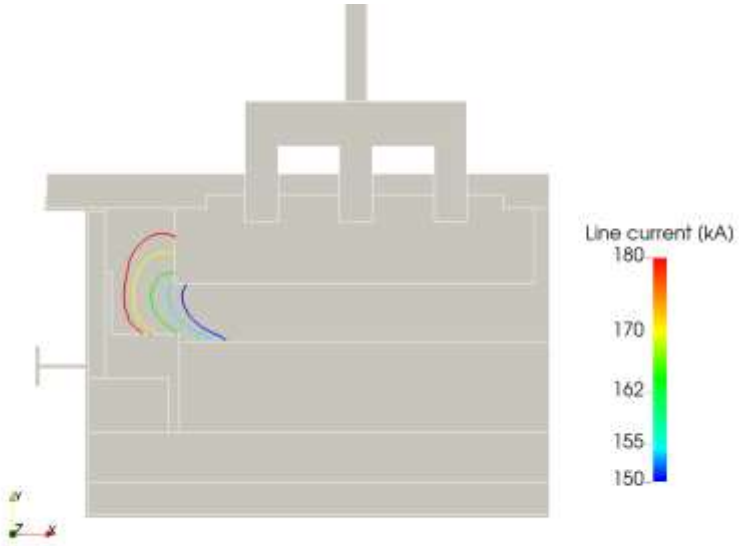

Figure 12. Numerical results of ledge position for different line currents.

Thus, the thermoelectric model can be utilized to predict the position of ledge, influence of various materials and geometries on the distribution of temperature, voltage and electric current densities. The model can be thus utilized to achieve optimizations with respect to thermoelectric fields. In the next step, simulation of complete 3D geometry of an industrial cell is planned through which validation of the model with an industrial cell can be achieved.

4. Conclusions

In the present work, the development of a numerical solver called "VirtualBatteryFoam" to simulate fully coupled complex physical phenomena in an aluminium cell is presented in two parts. The various numerical models namely, multiphase flows, electrodynamics, magneto-hydrodynamics, electrochemistry and thermoelectric fields to capture the physical phenomena occurring in the cell are detailed in the first part. In the second part, various phenomena are verified with experiments as follows:

- The long wave instability is simulated and validated with experiments from Pedchenko et al. [13].
- The production of CO_2 and its dynamics comprising of coalescence, build-up and release is compared with the experimental results of Zhao et al. [14] and was shown to be in good agreement.
- The influence of various line currents on the position of ledge boundary in a section of a fully detailed aluminium cell is presented, where the melting model is validated [11].

In the future, capturing the metal pad rolling of an industrial aluminium cell through simulations is planned. The interface position of liquid aluminium and liquid electrolyte will be compared between industry and numerical calculations. Additionally, the thermoelectric model will be combined with the MHD model to capture the thermal field and ledge position along with the amplitude of the metal pad and its velocity field. The electrochemistry simulations will be extended to capture the aluminium, carbon-dioxide and carbon-monoxide production in a real scale aluminium cell and the effect of release of gases on the anode-bath interface.

5. Acknowledgements

This research was funded by the German Ministry of Education and Research under the project SynErgie (No. 03SFK3B1), whose support is gratefully acknowledged. Additionally, the support of European Regional Development Fund (ERFE.NRW) and the state of Nordrhein-Westfalen is gratefully acknowledged. The authors would also like to thank the infrastructural support of the HPC cluster "Pleiades" at the University of Wuppertal.

6. References

1. Jomar Thonstad, Aluminium Electrolysis: Fundamentals of the Hall-Heroult Process, Aluminium-Verlag, 2001.
2. Kai Grjotheim und Halvor Kvande, *Introduction to Aluminium Electrolysis*, Alu media GmbH, 1993.
3. Andrea Prosperetti and Grétar Tryggvason, *Computational methods for multiphase flow*, Cambridge university press, 2007.
4. Henrik Rusche, Computational Fluid Dynamics of Dispersed Two-Phase Flows at High Phase Fractions, PhD Thesis, Imperial College, London, 2002.
5. Raad I. Issa, Solution of the Implicitly Discretized Fluid Flow Equations by Operator-Splitting, *Journal of Computational Physics*, 62 (1) 1986, 40-65.
6. Hrvoje Jasak, Error Analysis and Estimation for the Finite Volume Method with Applications to Fluid Flow, PhD Thesis, Department of Mechanical Engineering, Imperial College of Science, Technology, and Medicine, London, 1996, 146-152.
7. John D. Jackson, *Klassische Elektrodynamik*. de Gruyter, 2006.
8. R. Gutt et al., A numerical study of metal pad rolling instability in a simplified Hall–Héroult cell, *7th European Conference on Computational Fluid Dynamics*, Glasgow, 2018.
9. C. Swaminathan and V. Voller, A general enthalpy method for modeling solidification processes, *Metallurgical Transactions B: Process Metallurgy*, October 1992 Vol. 23 Issue 5, 651-664.
10. V.R. Voller and C. Prakash, Fixed grid numerical modelling methodology for convection-diffusion mushy region phase-change problems, *International Journal of Heat and Mass Transfer*, Vol. 30, Issue 8, 1987, 1709-1719, https://doi.org/10.1016/0017-9310(87)90317-6.
11. V. Nandana and U. Janoske, Experimental and numerical study on the melting behaviour of a phase change material in buoyancy driven flows, *7th European Conference on Computational Fluid Dynamics*, Glasgow, 2018.
12. Thorleif Sele, Instabilities of the metal surface in electrolytic alumina reduction cells, *Metallurgical Transactions B*, Vol 8 Issue 4, December 1977, 613–618. http://dx.doi.org/10.1007/bf02669338.
13. A. Pedchenko et al., Experimental model of the interfacial instability in aluminium reduction cells, EPL (*Europhysics Letters*) Vol. 88 No 2 3 November 2009, 24001, http://dx.doi.org/10.1209/0295-5075/88/24001.
14. Zhibin Zhao et al., Anodic bubble behavior and voltage drop in a laboratory transparent aluminum electrolytic cell, *Met and Mat Trans B* Vol 47, Issue 3, June 2016, 1962-1975, https://doi.org/10.1007/s11663-016-0598-9.